

Emergent half-metal with mixed structural order in (111)-oriented $(\text{LaMnO}_3)_2n|(\text{SrMnO}_3)_n$ superlattices

Fabrizio Cossu^{1,2,*}, Jlio Alves Do Nascimento^{1,2}, Stuart A. Cavill², Igor Di Marco^{2,3,4}, Vlado K. Lazarov², and Heung-Sik Kim^{1,†}

¹*Department of Physics and Institute of Quantum Convergence and Technology, Kangwon National University, Chuncheon 24341, Korea*

²*School of Physics, Engineering and Technology, University of York, Heslington, York YO10 5DD, England, United Kingdom*

³*Institute of Physics, Faculty of Physics, Astronomy and Informatics, Nicolaus Copernicus University, Grudziadzka 5, 87-100 Toru, Poland*

⁴*Department of Physics and Astronomy, Uppsala University, Box 516, SE-75120 Uppsala, Sweden*



(Received 31 October 2023; revised 18 December 2023; accepted 2 January 2024; published 26 January 2024)

Using first-principles techniques, we study the structural, magnetic, and electronic properties of (111)-oriented $(\text{LaMnO}_3)_2n|(\text{SrMnO}_3)_n$ superlattices of varying thickness ($n = 2, 4, 6$). We find that the properties of the thinnest superlattice ($n = 2$) are similar to the celebrated half-metallic ferromagnetic alloy $\text{La}_{2/3}\text{Sr}_{1/3}\text{MnO}_3$, with quenched Jahn-Teller distortions. At intermediate thickness ($n = 4$), the $a^-a^-a^-$ tilting pattern transitions to the $a^-a^-c^+$ tilting pattern, driven by the lattice degrees of freedom in the LaMnO_3 region. The emergence of the Jahn-Teller modes and the spatial extent needed for their development play a key role in this structural transition. For the largest thickness considered ($n = 6$), we unveil an emergent separation of Jahn-Teller and volume-breathing orders in the ground-state structure with the $a^-a^-c^+$ tilting pattern, whereas it vanishes in the antiferromagnetic configurations. The ground state of all superlattices is half-metallic ferromagnetic, not affected by the underlying series of structural transitions. Overall, these results outline a thickness-induced crossover between the physical properties of bulk $\text{La}_{2/3}\text{Sr}_{1/3}\text{MnO}_3$ and bulk LaMnO_3 .

DOI: [10.1103/PhysRevB.109.045435](https://doi.org/10.1103/PhysRevB.109.045435)

I. INTRODUCTION

Oxide thin films and superlattices hold great promise for future technologies, due to their remarkable versatility [1–3] and high-precision synthesis through advanced techniques such as molecular beam epitaxy [4–7] and pulsed laser deposition [8–13]. Among them, manganites have been under remarkable attention for potential applications in oxide electronics and spintronics thanks to the ferromagnetic (FM) phase, a high spin polarization, and the emergence of colossal magnetoresistance both in the bulk [14–20] and in superlattices [21–23]. A major goal for the research on manganite superlattices is to reach ferromagnetism and half-metallicity at high temperatures [24]. While the type of transport measurement determines whether true half-metallicity is observed [25] and defects, spin-orbit coupling, and temperature-dependent spin dynamics [26] have a non-negligible effect, it is accepted that the prediction of half-metallicity from temperature-free models represents a valuable insight [27,28]. Early theoretical and experimental studies focused on (001)-oriented mixed-valent manganite

superlattices [29–34]; (111)-oriented superlattices with LaMnO_3 [35–39] or SrMnO_3 [39,40] were also grown but remain underexplored due to difficulties in sample synthesis [41], especially concerning the SrMnO_3 side [39]. Nevertheless, (111)-oriented superlattices can host intriguing properties due to their symmetric character [42,43], a polar discontinuity at the interface [44–46], and a subtle competition between spin, orbital, charge, and lattice degrees of freedom.

Common compounds are LaMnO_3 and SrMnO_3 , respectively, an orthorhombic ($Pnma$ space group) Jahn-Teller (J-T) insulator with A-type antiferromagnetic (AFM) coupling, $a^-a^-c^+$ tilting system (in Glazer’s notation [47]) and Mott correlation and a cubic ($Pm\bar{3}m$) band insulator with G-type AFM coupling and negligible octahedral tilts. Their solid mixture with 1/3 Sr and 2/3 La is a rhombohedral ($R\bar{3}c$ space group [48]) half-metal with FM coupling, $a^-a^-a^-$ tilting system, and colossal magnetoresistance [17,49,50]. The $Pnma$ space group with the $a^-a^-c^+$ tilting system and the presence of the J-T distortions are crucial for the stability of the A-type AFM order of bulk LaMnO_3 [51–54]. Like other perovskite compounds, in superlattices we expect a competition of different tilting systems, charge and orbital orders, and various magnetic states; strain and stoichiometry provide a route to tune the tilting system [55,56] or to induce a crossover from orbital order to charge order [54,56,57]; magnetic phase transitions, coexistence, or separation may also occur [58–61]. *Ab initio* studies may be an outstanding instrument to determine the interplay of various degrees of freedom and predict emergent properties in superlattices. Our pilot study

*cossu@kangwon.ac.kr

†heungsikim@kangwon.ac.kr

on a (111)-oriented $(\text{LaMnO}_3)_{12}(\text{SrMnO}_3)_6$ superlattice with the $a^-a^-a^-$ tilting system revealed the presence of a robust half-metallic phase with rhombohedral symmetry that can be stabilized with a small in-plane compressive strain [56]. In this paper, we present the results of *ab initio* calculations of $(\text{LaMnO}_3)_{2n}(\text{SrMnO}_3)_n$ superlattices with $n = 2, 4, 6$. We provide a complete overview of structural, electronic, and magnetic properties against varying thickness, in the ground state (GS) as well as in excited states [62]. Our findings demonstrate the crucial role played by J-T distortions in the thickness-dependent structural transitions, as well as their connection to an emergent symmetry breaking between Mn sublattices within the $a^-a^-a^-$ tilting pattern.

II. METHODS AND MODELS

Density functional theory (DFT) calculations are performed using the projector-augmented wave method as implemented in the Vienna *ab initio* simulation package (VASP) [63,64]; the generalized gradient approximation (GGA) in the Perdew-Burke-Ernzerhof parametrization [65,66] is adopted. We used the pseudopotentials for Sr, La, Mn, and O which treat explicitly 10, 11, 15, and 6 electrons, respectively, and we chose an energy cutoff on the plane wave of 500 eV. The sampling of the Brillouin zone is performed with Γ -centred k meshes of $7 \times 4 \times 1$, $7 \times 4 \times 2$, and $7 \times 4 \times 3$ for the $n = 6, 4$, and 2 superlattices, respectively. In combination with it, a Gaussian smearing of 10 meV is used [except for the density of states (DOS), for which the tetrahedron method was adopted]. An energy tolerance of 1×10^{-6} eV and of 1×10^{-7} eV is adopted for the electronic loop during the structural optimization and the calculations of the electronic properties, respectively. Structures are considered relaxed with forces within 5×10^{-3} eVÅ⁻¹. The optimized lattice constant of 3.860 Å is in agreement with a previous study [56]. The Mn-3d states [67] are better described using the on-site repulsive correction via the rotationally invariant DFT+*U* approach [68], with Hubbard and Hund parameters $U = 3.8$ eV and $J = 1.0$ eV, respectively. These values are in line with previous work on (001)-oriented superlattices [56,69,70]. Moreover, we have recently demonstrated that calculations performed with the parameter-free metaGGA strongly constrained and appropriately normed (SCAN) functional [71] yield very similar results, confirming that the specific choice of U and J is not crucial for our scope [72]. The A-type, C-type, and G-type AFM orders, shown in Figs. 1(a)–1(c), are compared to the FM order (not illustrated). In the following, we will refer to these orders as A-AFM, C-AFM, and G-AFM, while we will use the term spin to indicate the spin magnetic moments. Full structural relaxation was performed to obtain the lattice parameters, based on energy and stress tensor minimization [56]. Crystallographic directions are defined by the Mn-O bonds and referred to as a , b , and c ; Cartesian axes x , y , and z are the two in-plane directions and the out-of-plane direction of the superlattice, respectively; crystallographic and Cartesian directions are illustrated in Figs. 1(d) and 1(e). In the (111) orientation, all three crystallographic directions a , b , and c have both in-plane and out-of-plane components, as opposed to (001) orientation, where two crystallographic axes lie on the in-plane direction while the third axis coincides

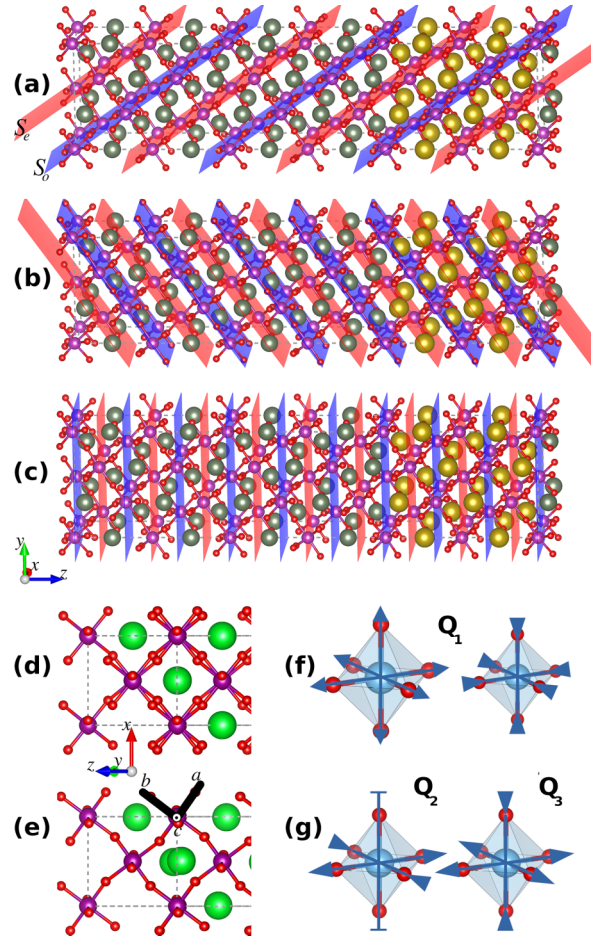


FIG. 1. Sketch of the structure of the superlattice, illustrating the magnetic orders and the tilting systems considered. The AFM A-type, C-type, and G-type orders are illustrated in (a), (b), and (c), respectively; blue and red planes highlight the two spin channels. The La, Sr, Mn, and O atoms are represented in dark green, yellow, purple, and red, respectively; in (d) and (e), A-site cations (La/Sr) are light green, whereas (f) and (g) show generic transition metal and its octahedral cage. The x , y , and z (the superlattice direction of growth) are along the crystallographic directions $(a/\sqrt{2}, -b/\sqrt{2}, 0)$, $(a/2, b/2, -c/\sqrt{2})$, and $(a/\sqrt{3}, b/\sqrt{3}, c/\sqrt{3})$, with axes in red, green, and blue, respectively. The tilts along the c crystallographic direction can be out of phase (d) and in phase (e). The main distortions considered in this paper are the v-b Q_1 (f) and the J-T Q_2 and Q_3 (g), with formulas defined in Ref. [56].

with the out-of-plane direction (the direction of growth). The rotation of the octahedra around the c axis is determined by the Mn-O-Mn angles. As octahedra are stacked along the c direction, these rotations can be either out of phase [Fig. 1(d)] or in phase [Fig. 1(e)] accounting for the $a^-a^-a^-$ and $a^-a^-c^+$ tilting systems, respectively [notice the superimposed positions of O lying along the a and b axes in Fig. 1(e) as opposed to Fig. 1(d)]. The volume-breathing (v-b) distortion Q_1 is illustrated in Fig. 1(f); the volume-conserving J-T distortions Q_2 and Q_3 are illustrated in Fig. 1(g). For the layer-resolved magnitudes of Q_1 , Q_2 , and Q_3 , we use the same notation formalized by Van Vleck and employed in previous work [54,56,73]; layered-resolved charge and spin distributions are computed according to Bader theory [74].

TABLE I. Relative energy of various magnetic states and tilting patterns, labeled with respect to the space group, of $(\text{LaMnO}_3)_2n|(\text{SrMnO}_3)_n$ superlattices with $n = 6, 4, 2$. Values are given in meV per formula unit and with respect to the ground state (GS) for any given n . The dashes for $n = 2$ in the $Pnma$ structure ($a^-a^-c^+$ tilting system) indicate that our calculations never converged to this arrangement, but always transitioned to the $R\bar{3}c$ structure ($a^-a^-a^-$ tilting system).

	$Pnma$				$R\bar{3}c$			
	FM	A-AFM	C-AFM	G-AFM	FM	A-AFM	C-AFM	G-AFM
$n = 6$ GS	26.46	43.79	72.16	7.62	37.53	53.84	95.60	
$n = 4$ GS	38.49	67.21	95.95	1.25	38.60	59.92	137.46	
$n = 2$					GS	47.11	80.98	109.41

Superlattices are built from the $Pnma$ and $R\bar{3}c$ bulk structures, featuring $a^-a^-c^+$ and $a^-a^-a^-$ tilting systems, respectively. Describing the former tilting system requires a doubling of the in-plane periodicity with respect to the latter one, for (111)-oriented superlattices; this corresponds to two formula units per layer. For an accurate comparison of energy with the same spacing of reciprocal lattice points, we nevertheless model the structure with $a^-a^-a^-$ tilting systems in the same $Pnma$ supercell. The La and Sr slabs alternate with thickness $2n$ and n , respectively, along the (111) direction, and n takes the values 2, 4, and 6. Only the $n = 6$ case is shown in Fig. 1 as the others are perfectly analogous. Odd values of the thickness would result in structural and magnetic frustration, and are not treated in the current paper.

Finally, the images of the structures are produced with VESTA JP-Minerals [75], and the analysis of the electronic properties is performed with the aid of the postprocessing code VASPKIT [76].

III. RESULTS

We start with the thickness-dependent structural and magnetic hierarchy illustrated in Table I. For all values of n , the magnetic ground state is FM, whereas the most competitive AFM order is A-AFM, which highlights the driving role played by LaMnO_3 ; further, the C-AFM and G-AFM follow in this order. A transition between the $a^-a^-a^-$ tilting pattern and the $a^-a^-c^+$ tilting pattern characterizes the structural order (see Table I) and determines some intriguing property, as we shall see below. For a comparison with LaMnO_3 and SrMnO_3 in the bulk, we point the reader to the results reported in Ref. [56] (supplemental material), where the A-AFM and the G-AFM orders are preferred to the FM order by 8.3 meV per formula unit and 99.2 meV per formula unit in bulk LaMnO_3 and bulk SrMnO_3 , respectively.

A. Structural properties and magnetic hierarchy

Naturally, the results for $n = 2$ are the closest to bulk $\text{La}_{2/3}\text{Sr}_{1/3}\text{MnO}_3$, in line with recent measurements of the magnetic and transport properties of (111)-oriented $(\text{LaMnO}_3)_2|(\text{SrMnO}_3)_1$ superlattices [39]. For such a small thickness, the $a^-a^-a^-$ tilting pattern is the ground state, whereas it is not even possible to stabilize the $a^-a^-c^+$ tilt-

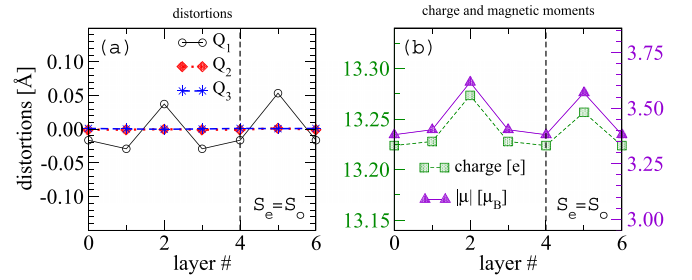


FIG. 2. Layer-resolved Van Vleck distortions (a) and charge and spin distributions (b) of the $n = 2$ superlattice, FM solution. The S_o and S_e sublattices show similar properties.

ing pattern as a metastable state. The octahedral distortions are virtually null, mirrored by a homogeneous distribution of charge and spin (see Fig. 2). Despite the difference in the chemical environment around the Mn between the SrMnO_3 region and the LaMnO_3 region, the Mn charge remains the same. In this scenario of valence states, the octahedra in the SrMnO_3 region tend to be larger than those in the LaMnO_3 region. Because of the symmetry, the two Mn atoms lying on the same layer are equivalent. With a notation which is explained in detail below, we indicate this fact by $S_e = S_o$. The magnetic order is FM, with a rather large energy gain with respect to the competing AFM orders (see Table I). We further notice that in Ref. [39] the SrMnO_3 layer has a Mn surrounded by Sr on one side and La on the other, whereas in the $n = 2$ case of the current paper there is a Mn layer surrounded by Sr on both sides.

As we increase the thickness of the superlattice, the ground state remains FM for all thicknesses and tilting patterns (see Table I). For a thickness larger than those we considered, we expect to recover bulk properties for both regions, namely a FM to A-AFM transition in the LaMnO_3 region and a FM to G-AFM transition in the SrMnO_3 region. A simulation of the mixed A-AFM/G-AFM order was performed to verify this hypothesis, finding an energy of 26.4 meV per formula unit above the ground state, meaning that such mixed order is still unfavorable at $n = 6$. Additionally, a mixed A-AFM/FM order was simulated, finding an energy of 26.8 meV per formula unit above the ground state. Therefore, with the A-AFM order in the LaMnO_3 regions and FM, G-AFM, and A-AFM in the SrMnO_3 region (compare also with Table I), a negligible energy cost is found for a FM-AFM transition in the SrMnO_3 region. This is due to the close and subtle competition between FM and AFM exchange coupling revealed in our previous work [56]. This competition also suggests that the FM to G-AFM transition in the SrMnO_3 region is likely to be preceded by local spin flips, which is consistent with the fact that bulk SrMnO_3 is a wide-gap band insulator.

Moving to the structural analysis, and as mentioned above, Table I shows that increasing thickness from $n = 2$ to 4 induces a change of tilting pattern, from $a^-a^-a^-$ to $a^-a^-c^+$. The thicker superlattice allows for more variability in the plots of the lattice distortions and the charge/spin distributions across the layers, illustrated in Fig. 3. With hindsight, we can group the Mn sites into two distinct sublattices, depicted as alternating blue and red (001) planes in Fig. 1(a) and labeled as S_o and S_e , respectively [77]. Despite the fact that these

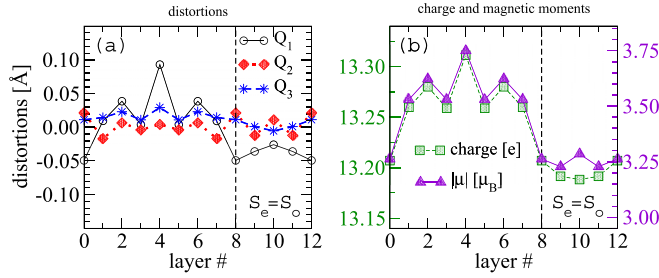


FIG. 3. Layer-resolved Van Vleck distortions (a) and charge and spin distributions (b) of the $n = 4$ superlattice, FM solution. The S_o and S_e sublattices show similar properties.

sublattices are different by symmetry the results obtained for $n = 4$ show a quasidegeneracy, for all magnetic orders. Therefore, only one set of curves is reported in Fig. 3, for a clearer visualization. These data show that, for $n = 4$, the Q_1 v-b distortion in the FM ground state dominates over the J-T distortions, still quenched. The suppression of the J-T distortions here is not a mere consequence of the tilting system [78,79] and the small LaMnO_3 thickness, but is an effect of the magnetic degrees of freedom. In fact, the J-T distortions emerge in the A-AFM solution, as illustrated by Fig. 4. This is particularly evident for Q_2 , as it is linked to the orbital order along the [001] planes, likely promoting FM coupling therein. These findings are consistent with the fact that J-T distortions are necessary for the formation of the A-AFM order [51–54]. Going back to the analysis of Fig. 3, volume, charge, and spin oscillate in the LaMnO_3 region, featuring a peak in the innermost layer; the v-b Q_1 distortion is mirrored by the layered-resolved charge/spin distribution, as previously reported for the $a^-a^-a^-$ tilting pattern ($n = 6$) [56]. In the center of the SrMnO_3 region, volume and spin reach a peak, whereas the charge varies more smoothly. This demonstrates the complex interplay between the various degrees of freedom which prevents a simple picture based on the assumption of a homogeneous charge transfer.

We now move to the data for $n = 6$, which is the largest thickness we study. Figure 5 shows the distribution of layered-resolved Van Vleck distortions, charge, and spin of the FM ground state. In contrast with the $n = 4$ case, a dramatic difference arises between the sublattices S_o and S_e . The v-b Q_1 distortion is still mirrored by the layered-resolved charge/spin distribution [compare Fig. 5(a) with Fig. 5(c) and Fig. 5(b) with Fig. 5(d)]. Moreover, we now have marked J-T dis-

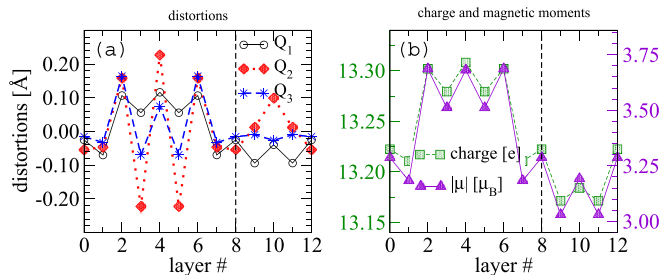


FIG. 4. Layer-resolved Van Vleck distortions (a) and charge and spin distributions (b) of the $n = 4$ superlattice, A-AFM solution. The S_o and S_e sublattices show similar properties.

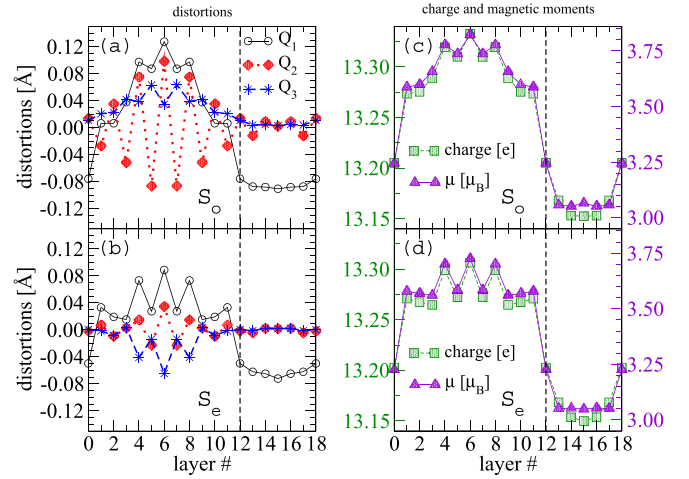


FIG. 5. Layer-resolved structural and electronic/magnetic properties of the ground state of the $n = 6$ superlattice, the FM solution with the $a^-a^-c^+$ tilting pattern: Van Vleck distortions in sublattice S_o (a) and S_e (b); charge and spin distributions in sublattices S_o (c) and S_e (d).

tortions for the FM ground state. The J-T Q_2 distortion is obviously accompanied by orbital order [52,80]. The largest contributions to Q_2 arise mainly from the S_o sublattice [see Fig. 5(a)], while these modes seem quenched in the S_e sublattice [see Fig. 5(b)].

The relative weight of the Q_1 mode is particularly large in the S_e sublattice, while it is comparable to Q_2 for S_o . Moreover, Q_1 exhibits oscillations in the S_e sublattice, while it varies smoothly in the S_o sublattice. Therefore, also for Q_1 we observe a qualitative difference across the two sublattices, which is connected to the charge distribution. The larger charge in the S_o sublattice [see Fig. 5(c)] points to a larger La-Sr valence separation therein and suggests a propensity of the S_o sublattice to restore the bulklike orbital order and the J-T distortions, by withstanding the interfacial charge transfer from LaMnO_3 to SrMnO_3 . Such valence separation is crucial for the emergence of mixed structural features, because a valence closer to $3+$ drives the e_g occupation closer to $1/2$, prompting J-T distortions. On the other hand, opposite values of the Q_3 distortion and different charge states in the LaMnO_3 region for the two sublattices promote a FM coupling along (001) within the Goodenough-Kanamori model [81–83]. Note that the hopping between two sublattices occurs not along the same layer (same z value), but between adjacent layers.

We proceed to the analysis of the A-AFM order for $n = 6$. The Van Vleck distortions and the charge/spin distribution are illustrated in Fig. 6. The curves for S_o and S_e sublattices are virtually equivalent, and therefore only one set of curves is shown. Analogously to the $n = 4$ case, the Q_2 distortion in the A-AFM solution is larger than that in the FM ground state and arises in the LaMnO_3 region, unsurprisingly. The Q_3 distortion oscillates between positive and negative values, with a small amplitude, and peaks at the interfaces. In contrast with the FM solution, Q_1 changes abruptly at the interface but does not show oscillations within either bulk region [see Fig. 6(a)]; again, the Q_1 distortion is mirrored by charge/spin oscillations [see Fig. 6(b)].

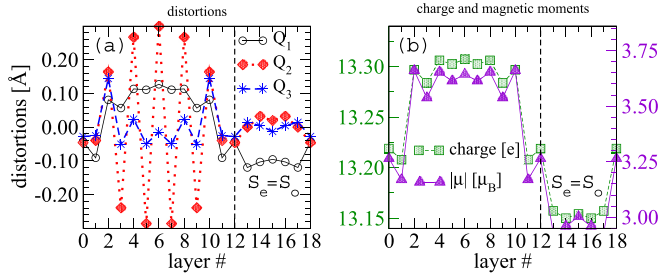


FIG. 6. Layer-resolved Van Vleck distortions (a) and charge and spin distributions (b) of the $n = 6$ superlattice, A-AFM solution. The S_o and S_e sublattices show similar properties.

Further calculations, for example the analysis of the structural distortions of the C-AFM, reveal that the quasiequivalence between S_e and S_o sublattices does not depend on the type of AFM order; therefore, as illustrated in Fig. 7, we show only one set. While in the FM solution single-spin sublattices display a broken structural symmetry; if the spin is compelled to adopt two distinct states the lattice degrees of freedom adjust and relax to a single-phase configuration.

B. Electronic properties

For every thickness, the FM solution features a half-metallic state which persists across all the layers of the superlattice, as shown by the projected density of states (PDOS) in Fig. 8. The A-AFM solution is instead fully insulating with a band gap across the e_g states. Such gap is constant throughout the superlattice for $n = 2$ and 4, whereas it is enhanced in the LaMnO₃ region for $n = 6$. In particular, it amounts to ≈ 0.16 , ≈ 0.22 and 0.56 eV for $n = 2$, 4, and 6 (LaMnO₃ region), respectively. These values are well below the value of ≈ 1.2 eV calculated for bulk LaMnO₃, confirming that the relaxation to an insulating AFM phase (bulklike) may happen only at a larger thickness. This reflects a spatially extended charge transfer between Sr and La regions, which is also evident from the charge densities (data not shown) and the plots of the Bader charges. Overall, these features are fully consistent with recent data for (111)-oriented LaAlO₃/SrTiO₃ superlattices [45]. In connection with the aforementioned FM-AFM transition, expected at large n , this charge distribution will cease extending and eventually recede when the system becomes insulating.

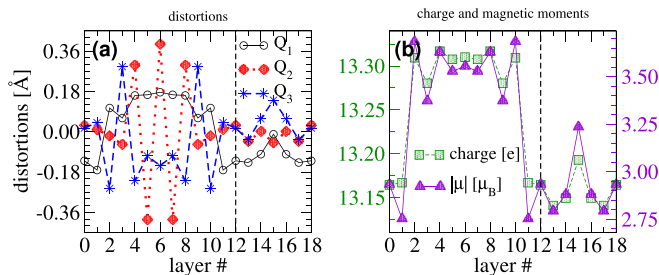


FIG. 7. Layer-resolved Van Vleck distortions (a) and charge and spin distributions (b) of the $n = 6$ superlattice, C-AFM solution. The S_o and S_e sublattices show similar properties.

Furthermore, we observe that the character of the bands in both the FM and the A-AFM solution slightly changes with thickness. In fact, a gap between the t_{2g} states and e_g states exists in all regions (LaMnO₃, interface, SrMnO₃) for $n = 2$, whereas it is present only in the LaMnO₃ region for $n = 4$ and 6 (see the DOS in Fig. 8); such trend is seen for both FM and A-AFM solutions. On the other hand, a residual t_{2g} - e_g mixing is observed in the LaMnO₃ region, which can reflect the octahedral distortions as seen in Figs. 2–6.

We notice that our computational approach may neglect effects that are detrimental to the half-metallic character we predict in this family of superlattices. For example, we do not include spin-orbit coupling nor do we investigate the occurrence of noncollinear magnets; this latter would mix the two spin channels and decrease spin polarization of the carriers [84,85]. Moreover, we do not include explicit many-body effects, which may lead to nonquasiparticle states forming inside the minority-spin band gap [26]. While these effects go beyond the scope of the present paper, which we expect to be unaffected in terms of structural and magnetic hierarchy, as well as excitation spectra, one should also stress that deviations from a full spin polarization may become larger and much more relevant in transport properties, depending on the type of measurement [25].

IV. DISCUSSION AND CONCLUSIONS

The main results of the current paper are the evolution of properties with thickness—showing that Jahn-Teller distortions kick in before the metal-insulator transition or the FM-AFM transition—and the relation of the structural and spin degrees of freedom—showing a sublattice separation of structural phases in the spin-degenerate FM ground state and that the sublattices become (quasi)degenerate in structural properties when the spin degeneracy is lifted. The former result highlights the primary role played by the J-T distortions originating from the LaMnO₃ region of the superlattice; the latter points to a symmetry-dependent separation—it occurs only in presence of the $a^-a^-c^+$ tilting pattern—which is realized on either of the lattice or spin degrees of freedom. The fact that J-T distortions in the FM phase are sizable for $n = 6$, but dramatically quenched for $n = 4$, is interpreted as a precursor of the transition to a different tilting pattern, which happens for $n = 2$.

An interesting question arising from our paper is on the emergence of the separation of J-T and v-b sublattices and its connection to magnetism. Our most plausible explanation is drawn in the light of an antagonism between the A-AFM magnetic order of the LaMnO₃—promoted by J-T and the $a^-a^-c^+$ tilting pattern—and the FM order of the superlattice—promoted by strain and charge transfer. While in the $a^-a^-a^-$ tilting pattern the J-T distortions are naturally suppressed by symmetry [78,86], as the thickness increases and the tilting pattern of bulk LaMnO₃ is adopted, the J-T distortions appear in the AFM solutions. For the largest thickness considered, while the FM order is still preferred, the tilting pattern tends to promote J-T distortions but cannot maximize them via an insulating A-AFM order because such state is not energetically competitive. Thus, the system adopts a mixed configuration: in one sublattice, the J-T are stronger and in

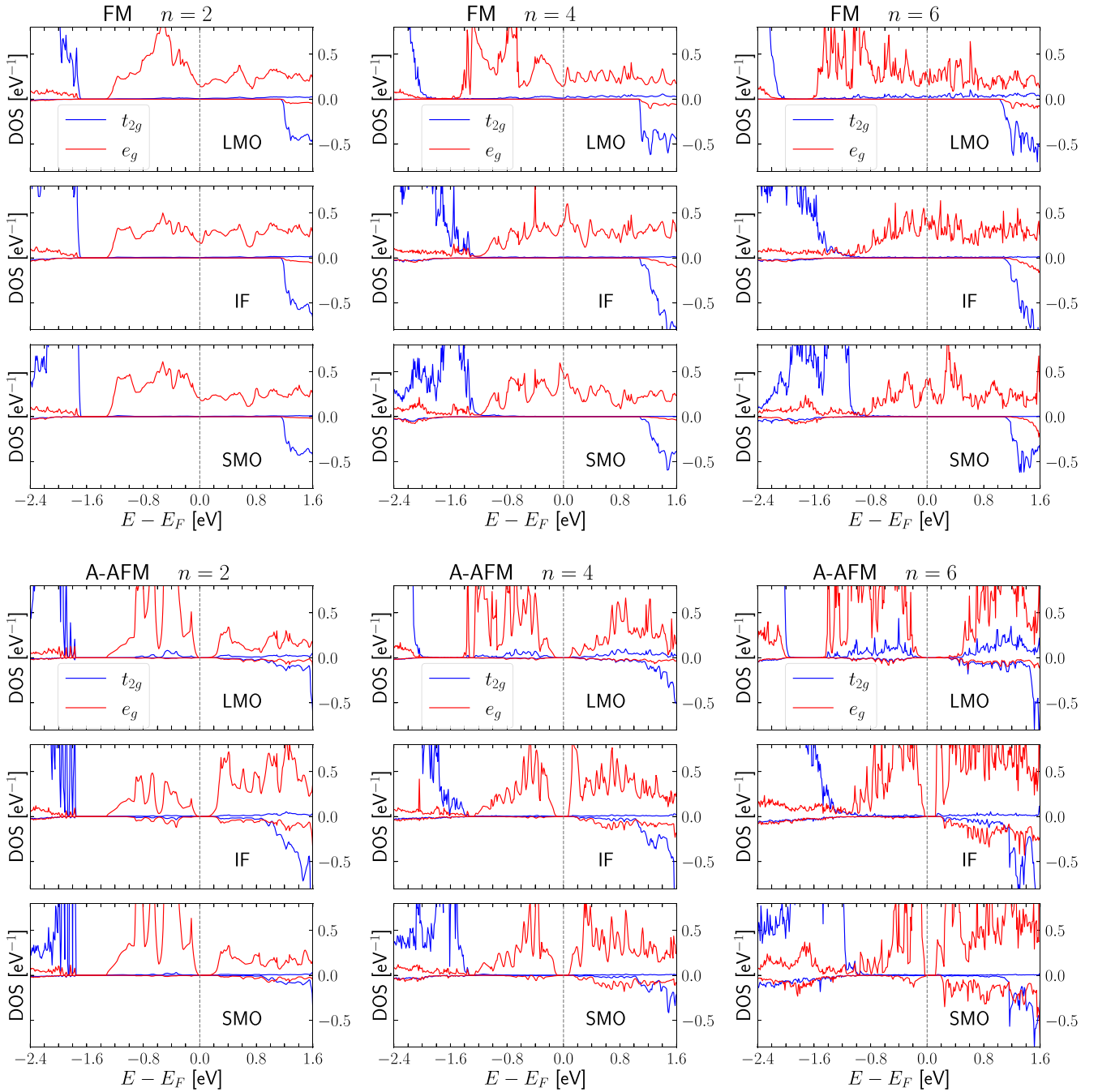


FIG. 8. Layer-resolved PDOS of the $n = 2, 4$, and 6 superlattices, FM, and A-AFM solution. For all systems, we represent the central layer of the LaMnO_3 region (LMO), the layer at the interface (IF), and the central layer of the SrMnO_3 region (SMO).

the other they are weaker and overshadowed by the v-b. This interpretation also suggests why the two sublattices remain degenerate for $n = 4$ even in the FM solution: there is not enough room for the above-mentioned competition to develop along the direction of growth.

A broader connection to the analysis above is provided by existing measurements and models for bulk LaMnO_3 . On one hand, Raman spectra [20] and magnetotransport measurements [87] show the occurrence of a phase separation, where J-T regions are sided by regions with no J-T, under a moderate hydrostatic pressure. On the other hand,

ab initio calculations show a (hidden) competition between Van Vleck modes Q_2 (J-T) and Q_1 (v-b) [54]. We advance the hypothesis that in (111)-oriented mixed-valent superlattices, a combination of strain and charge transfer parallel the moderate hydrostatic pressure causing the aforementioned phase separation. Further investigations based on scanning transmission electron microscopy (STEM) could verify the actual realization and character of structural features—such as octahedral tilts—which are deeply linked to electronic and magnetic properties according to our predictions. In addition, orbital occupations (at the interfaces) may be investigated

using x-ray magnetic linear dichroism (XMLD) in reflectivity. We also note that epitaxial strain may tune the structural phase separation observed in the current paper, as it does not occur with the $a^-a^-a^-$ tilting pattern which is favored by a range of substrates.

Finally, our results support the importance of symmetry in the description of electronic properties and electronic correlations, as recent research work [78,79,86,88] has highlighted. Since v-b (J-T) distortions are linked to the emergence of Hund (Mott) correlations [57,78], further research on these and similar superlattices is expected to unveil the strong intertwining between Mott and Hund physics. In this sense, similar systems, often showing Hund-driven charge disproportionation, are nickelates [57,89–93] and ruthenates [94–96].

Concluding, we presented an *ab initio* study on (111)-oriented $(\text{LaMnO}_3)_{2n}(\text{SrMnO}_3)_n$ superlattices with $n = 2, 4, 6$. All studied systems exhibit a robust half-metallic FM order, persistent across all the layers. We observe a crossover between bulk $\text{La}_{2/3}\text{Sr}_{1/3}\text{MnO}_3$ and bulk LaMnO_3 with varying thickness, where the J-T distortions play a crucial role. In the *Pnma* structure, the FM GS consists of two sublattices with qualitatively different Van Vleck distortions and charge/spin distributions. These sublattices become quasidegenerate for all AFM orders, which are also accompanied by growing J-T distortions. These findings highlight the complex and fascinating relationship between lattice, charge, orbital, and spin degrees of freedom in (111)-oriented manganite superlattices, and underscore their potential for novel functionalities and applications.

ACKNOWLEDGMENTS

We are thankful to I. I. Mazin, A. Edström, and A. Akbari for valuable discussions. The computational resources were provided by the Korean Institute of Science and Technology Information (KISTI) national supercomputing center (Project No. KSC-2022-CRE-0358), by the National Academic Infrastructure for Supercomputing in Sweden (NAISS) and the Swedish National Infrastructure for Computing (SNIC) at the Center for High Performance Computing (PDC) in Stockholm, Sweden, partially funded by the Swedish Research Council through Grants No. 2022-06725 and No. 2018-05973; we additionally appreciate the computational support from the University of York High-Performance Computing service, Viking, and the Research Computing team. F.C., H.-S.K., and I.D.M. acknowledge financial support from the National Research Foundation (NRF) funded by the Ministry of Science of Korea (Grants No. 2022R1I1A1A01071974, No. 2020R1C1C1005900, and No. 2020R1A2C101217411, respectively). H.-S.K. acknowledges additional support from the international cooperation program managed by the National Research Foundation of Korea (NRF, Grant No. NRF-2023K2A9A2A12000317). I.D.M. acknowledges financial support from the European Research Council (ERC), Synergy Grant FASTCORR, Project No. 854843. This research is also part of Project No. 2022/45/P/ST3/04247 cofunded by the National Science Centre and the European Union's Horizon 2020 research and innovation program under the Marie Skłodowska-Curie Grant No. 945339.

- [1] E. R. Hoglund, D.-L. Bao, A. O'Hara, S. Makarem, Z. T. Piontkowski, J. R. Matson, A. K. Yadav, R. C. Haislmaier, R. Engel-Herbert, J. F. Ihlefeld, J. Ravichandran, R. Ramesh, J. D. Caldwell, T. E. Beechem, J. A. Tomko, J. A. Hachtel, S. T. Pantelides, P. E. Hopkins, and J. M. Howe, Emergent interface vibrational structure of oxide superlattices, *Nature (London)* **601**, 556 (2022).
- [2] Y. Jia, R. V. Chopdekar, E. Arenholz, Z. Liu, M. D. Biegalski, Z. D. Porter, A. Mehta, and Y. Takamura, Thickness dependence of exchange coupling in (111)-oriented perovskite oxide superlattices, *Phys. Rev. B* **93**, 104403 (2016).
- [3] C. Yang, R. A. Ortiz, Y. Wang, W. Sigle, H. Wang, E. Benckiser, B. Keimer, and P. A. van Aken, Thickness-dependent interface polarity in infinite-layer nickelate superlattices, *Nano Lett.* **23**, 3291 (2023).
- [4] A. Prakash and B. Jalan, Molecular beam epitaxy for oxide electronics, *Molecular Beam Epitaxy* (John Wiley & Sons, Ltd, 2019), Chap. 26, pp. 423–452.
- [5] S. Ismail-Beigi, F. J. Walker, A. S. Disa, K. M. Rabe, and C. H. Ahn, Picoscale materials engineering, *Nat. Rev. Mater.* **2**, 17060 (2017).
- [6] J. Roth, T. Kuznetsova, L. Miao, A. Pogrebnjakov, N. Alem, and R. Engel-Herbert, Self-regulated growth of [111]-oriented perovskite oxide films using hybrid molecular beam epitaxy, *APL Mater.* **9**, 021114 (2021).
- [7] V. K. Lazarov, Z. Cai, K. Yoshida, K. H. L. Zhang, M. Weinert, K. S. Ziemer, and P. J. Hasnip, Dynamically stabilized growth of polar oxides: The case of $\text{MgO}(111)$, *Phys. Rev. Lett.* **107**, 056101 (2011).
- [8] M. Lorenz, Pulsed laser deposition, *Digital Encyclopedia of Applied Physics* (John Wiley & Sons, Ltd, 2019), pp. 1–29.
- [9] G. Eres, J. Z. Tischler, C. M. Rouleau, H. N. Lee, H. M. Christen, P. Zschack, and B. C. Larson, Dynamic scaling and island growth kinetics in pulsed laser deposition of SrTiO_3 , *Phys. Rev. Lett.* **117**, 206102 (2016).
- [10] X. Yao, C. W. Schneider, T. Lippert, and A. Wokaun, Manipulation of ion energies in pulsed laser deposition to improve film growth, *Appl. Phys. A* **125**, 344 (2019).
- [11] G. Koster, D. H. A. Blank, and G. A. J. H. M. Rijnders, Oxygen in complex oxide thin films grown by pulsed laser deposition: A perspective, *J. Supercond. Novel Magn.* **33**, 205 (2020).
- [12] D. Cheshire, P. Bencok, D. Gianolio, G. Cibin, V. K. Lazarov, G. van der Laan, and S. A. Cavill, Absence of spin-mixed states in ferrimagnet Yttrium iron garnet, *J. Appl. Phys.* **132**, 103902 (2022).
- [13] D. Gilks, K. P. McKenna, Z. Nedelkoski, B. Kuerbanjiang, K. Matsuzaki, T. Susaki, L. Lari, D. Kepaptsoglou, Q. Ramasse, S. Tear, and V. K. Lazarov, Polar spinel-perovskite interfaces: an atomistic study of $\text{Fe}_3\text{O}_4(111)/\text{SrTiO}_3(111)$ structure and functionality, *Sci. Rep.* **6**, 29724 (2016).
- [14] Z. Sun, Q. Wang, J. F. Douglas, H. Lin, S. Sahrakorpi, B. Barbiellini, R. S. Markiewicz, A. Bansil, A. V. Fedorov, E. Rotenberg, H. Zheng, J. F. Mitchell, and D. S. Dessau, Minority-spin t_{2g} states and the degree of spin polarization in

- ferromagnetic metallic $\text{La}_{2-2x}\text{Sr}_{1+2x}\text{Mn}_2\text{O}_7$ ($x = 0.38$), *Sci. Rep.* **3**, 3167 (2013).
- [15] B. Prasad, W. Zhang, J. Jian, H. Wang, and M. G. Blamire, Strongly bias-dependent tunnel magnetoresistance in manganese spin filter tunnel junctions, *Adv. Mater.* **27**, 3079 (2015).
- [16] Y. Tokura, Critical features of colossal magnetoresistive manganites, *Rep. Prog. Phys.* **69**, 797 (2006).
- [17] Y. Tokura and Y. Tomioka, Colossal magnetoresistive manganites, *J. Magn. Magn. Mater.* **200**, 1 (1999).
- [18] E. Dagotto, Open questions in CMR manganites, relevance of clustered states and analogies with other compounds including the cuprates, *New J. Phys.* **7**, 67 (2005).
- [19] E. Dagotto, T. Hotta, and A. Moreo, Colossal magnetoresistant materials: The key role of phase separation, *Phys. Rep.* **344**, 1 (2001).
- [20] M. Baldini, V. V. Struzhkin, A. F. Goncharov, P. Postorino, and W. L. Mao, Persistence of Jahn-Teller distortion up to the insulator to metal transition in LaMnO_3 , *Phys. Rev. Lett.* **106**, 066402 (2011).
- [21] H. Nakao, T. Sudayama, M. Kubota, J. Okamoto, Y. Yamasaki, Y. Murakami, H. Yamada, A. Sawa, and K. Iwasa, Magnetic and electronic states in $(\text{LaMnO}_3)_2(\text{SrMnO}_3)_2$ superlattice exhibiting a large negative magnetoresistance, *Phys. Rev. B* **92**, 245104 (2015).
- [22] T. Miao, L. Deng, W. Yang, J. Ni, C. Zheng, J. Etheridge, S. Wang, H. Liu, H. Lin, Y. Yu, Q. Shi, P. Cai, Y. Zhu, T. Yang, X. Zhang, X. Gao, C. Xi, M. Tian, X. Wu, H. Xiang *et al.*, Direct experimental evidence of physical origin of electronic phase separation in manganites, *Proc. Natl. Acad. Sci. USA* **117**, 7090 (2020).
- [23] V. Gayathri, E. P. Amaladass, A. T. Sathyanarayana, T. G. Kumary, R. Pandian, P. Gupta, S. K. Rai, and A. Mani, Interfacial interaction driven enhancement in the colossal magnetoresistance property of ultra-thin heterostructure of $\text{Pr}_{0.6}\text{Sr}_{0.4}\text{MnO}_3$ in proximity with $\text{Pr}_{0.5}\text{Ca}_{0.5}\text{MnO}_3$, *Sci. Rep.* **13**, 2315 (2023).
- [24] A.-M. Haghiri-Gosnet and J.-P. Renard, CMR manganites: Physics, thin films and devices, *J. Phys. D* **36**, R127 (2003).
- [25] B. Nadgorny, I. I. Mazin, M. Osofsky, R. J. Soulen, P. Broussard, R. M. Stroud, D. J. Singh, V. G. Harris, A. Arsenov, and Y. Mukovskii, Origin of high transport spin polarization in $\text{La}_{0.7}\text{Sr}_{0.3}\text{MnO}_3$: Direct evidence for minority spin states, *Phys. Rev. B* **63**, 184433 (2001).
- [26] M. I. Katsnelson, V. Y. Irkhin, L. Chioncel, A. I. Lichtenstein, and R. A. de Groot, Half-metallic ferromagnets: From band structure to many-body effects, *Rev. Mod. Phys.* **80**, 315 (2008).
- [27] X. Li and J. Yang, First-principles design of spintronics materials, *Natl. Sci. Rev.* **3**, 365 (2016).
- [28] Q. Tang and X. Zhu, Half-metallic double perovskite oxides: recent developments and future perspectives, *J. Mater. Chem. C* **10**, 15301 (2022).
- [29] C. Adamo, C. A. Perroni, V. Cataudella, G. De Filippis, P. Orgiani, and L. Maritato, Tuning the metal-insulator transitions of $(\text{SrMnO}_3)_n/(\text{LaMnO}_3)_{2n}$ superlattices: Role of interfaces, *Phys. Rev. B* **79**, 045125 (2009).
- [30] A. Bhattacharya, S. J. May, S. G. E. te Velthuis, M. Warusawithana, X. Zhai, B. Jiang, J.-M. Zuo, M. R. Fitzsimmons, S. D. Bader, and J. N. Eckstein, Metal-insulator transition and its relation to magnetic structure in $(\text{LaMnO}_3)_{2n}/(\text{SrMnO}_3)_n$ superlattices, *Phys. Rev. Lett.* **100**, 257203 (2008).
- [31] B. R. K. Nanda and S. Satpathy, Electronic and magnetic structure of the $(\text{LaMnO}_3)_{2n}/(\text{SrMnO}_3)_n$ superlattices, *Phys. Rev. B* **79**, 054428 (2009).
- [32] S. Smadici, P. Abbamonte, A. Bhattacharya, X. Zhai, B. Jiang, A. Rusydi, J. N. Eckstein, S. D. Bader, and J.-M. Zuo, Electronic reconstruction at SrMnO_3 - LaMnO_3 superlattice interfaces, *Phys. Rev. Lett.* **99**, 196404 (2007).
- [33] S. Dong, R. Yu, S. Yunoki, G. Alvarez, J.-M. Liu, and E. Dagotto, Magnetism, conductivity, and orbital order in $(\text{LaMnO}_3)_{2n}/(\text{SrMnO}_3)_n$ superlattices, *Phys. Rev. B* **78**, 201102(R) (2008).
- [34] H. Chen and A. Millis, Charge transfer driven emergent phenomena in oxide heterostructures, *J. Phys.: Condens. Matter* **29**, 243001 (2017).
- [35] F. Y. Bruno, M. Gibert, S. McKeown Walker, O. E. Peil, A. de la Torre, S. Riccò, Z. Wang, S. Catalano, A. Tamai, F. Bisti, V. N. Strocov, J.-M. Triscone, and F. Baumberger, Electronic structure of buried lanio3 layers in (111)-oriented $\text{LaNiO}_3/\text{LaMnO}_3$ superlattices probed by soft x-ray arpes, *APL Mater.* **5**, 016101 (2017).
- [36] J. Zang, G. Zhou, Y. Bai, Z. Quan, and X. Xu, The exchange bias of $\text{LaMnO}_3/\text{LaNiO}_3$ superlattices grown along different orientations, *Sci. Rep.* **7**, 10557 (2017).
- [37] M. Gibert, P. Zubko, R. Scherwitzl, J. Íñiguez, and J.-M. Triscone, Exchange bias in LaNiO_3 - LaMnO_3 superlattices, *Nat. Mater.* **11**, 195 (2012).
- [38] H. Wei, M. Grundmann, and M. Lorenz, Confinement-driven metal-insulator transition and polarity-controlled conductivity of epitaxial $\text{LaNiO}_3/\text{LaAlO}_3$ (111) superlattices, *Appl. Phys. Lett.* **109**, 082108 (2016).
- [39] Z. Wang, Q. An, M. Meng, W. Xue, J. Bi, Y. Cao, Y. Wang, X. Liu, F. Yang, and J. Guo, Effect of a-site cation ordering on the electrical and magnetic properties of manganite films, *Phys. Status Solidi B* **259**, 2100564 (2022).
- [40] R.-N. Song, M.-H. Hu, X.-R. Chen, and J.-D. Guo, Epitaxial growth and thermostability of cubic and hexagonal SrMnO_3 films on SrTiO_3 (111), *Front. Phys.* **10**, 321 (2015).
- [41] Y. A. Mantz, New LaMnO_3 surface energy results obtained from density-functional theory, *Surf. Sci.* **695**, 121500 (2020).
- [42] A. Rüegg, C. Mitra, A. A. Demkov, and G. A. Fiete, Lattice distortion effects on topological phases in $(\text{LaNiO}_3)_2/(\text{LaAlO}_3)_N$ heterostructures grown along the [111] direction, *Phys. Rev. B* **88**, 115146 (2013).
- [43] A. Rüegg, C. Mitra, A. A. Demkov, and G. A. Fiete, Electronic structure of $(\text{LaNiO}_3)_2/(\text{LaAlO}_3)_N$ heterostructures grown along [111], *Phys. Rev. B* **85**, 245131 (2012).
- [44] J. Chakhalian, A. J. Millis, and J. Rondinelli, Whither the oxide interface, *Nat. Mater.* **11**, 92 (2012).
- [45] K. Song, S. Ryu, H. Lee, T. R. Paudel, C. T. Koch, B. Park, J. K. Lee, S.-Y. Choi, Y.-M. Kim, J. C. Kim, H. Y. Jeong, M. S. Rzechowski, E. Y. Tsybal, C.-B. Eom, and S. H. Oh, Direct imaging of the electron liquid at oxide interfaces, *Nat. Nanotechnol.* **13**, 198 (2018).
- [46] S. Ryu, H. Zhou, T. R. Paudel, N. Campbell, J. Podkaminer, C. W. Bark, T. Hernandez, D. D. Fong, Y. Zhang, L. Xie, X. Q. Pan, E. Y. Tsybal, M. S. Rzechowski, and C. B. Eom, Electronic reconstruction at the polar (111)-oriented oxide interface, *APL Mater.* **10**, 031115 (2022).

- [47] A. M. Glazer, The classification of tilted octahedra in perovskites, *Acta Crystallogr. Sect. B* **28**, 3384 (1972).
- [48] M. Saleem and D. Varshney, Structural, thermal, and transport properties of $\text{La}_{0.67}\text{Sr}_{0.33}\text{MnO}_3$ nanoparticles synthesized via the sol-gel auto-combustion technique, *RSC Adv.* **8**, 1600 (2018).
- [49] Y. Tokura, A. Urushibara, Y. Moritomo, T. Arima, A. Asamitsu, G. Kido, and N. Furukawa, Giant magnetotransport phenomena in filling-controlled kondo lattice system: $\text{La}_{1-x}\text{Sr}_x\text{MnO}_3$, *J. Phys. Soc. Jpn.* **63**, 3931 (1994).
- [50] M. Imada, A. Fujimori, and Y. Tokura, Metal-insulator transitions, *Rev. Mod. Phys.* **70**, 1039 (1998).
- [51] W. E. Pickett and D. J. Singh, Electronic structure and half-metallic transport in the $\text{La}_{1-x}\text{Ca}_x\text{MnO}_3$ system, *Phys. Rev. B* **53**, 1146 (1996).
- [52] J. Geck, P. Wochner, S. Kiele, R. Klingeler, A. Revcolevschi, M. von Zimmermann, B. Büchner, and P. Reutler, Orbital order induced ferromagnetic insulating properties, *New J. Phys.* **6**, 152 (2004).
- [53] E. Pavarini and E. Koch, Origin of Jahn-Teller distortion and orbital order in LaMnO_3 , *Phys. Rev. Lett.* **104**, 086402 (2010).
- [54] M. M. Schmitt, Y. Zhang, A. Mercy, and P. Ghosez, Electron-lattice interplay in LaMnO_3 from canonical Jahn-Teller distortion notations, *Phys. Rev. B* **101**, 214304 (2020).
- [55] F. Cossu, H. A. Tahini, N. Singh, and U. Schwingenschlögl, Charge driven metal-insulator transitions in $\text{LaMnO}_3/\text{SrTiO}_3$ (111) superlattices, *Europhys. Lett.* **118**, 57001 (2017).
- [56] F. Cossu, H.-S. Kim, B. Sanyal, and I. Di Marco, Persistent half-metallic ferromagnetism in a (111)-oriented manganite superlattice, *npj Comput. Mater.* **8**, 77 (2022).
- [57] I. I. Mazin, D. I. Khomskii, R. Lengsdorf, J. A. Alonso, W. G. Marshall, R. M. Ibberson, A. Podlesnyak, M. J. Martínez-Lope, and M. M. Abd-Elmeguid, Charge ordering as alternative to Jahn-Teller distortion, *Phys. Rev. Lett.* **98**, 176406 (2007).
- [58] A. Tebano, C. Aruta, S. Sanna, P. G. Medaglia, G. Balestrino, A. A. Sidorenko, R. De Renzi, G. Ghiringhelli, L. Braicovich, V. Bisogni, and N. B. Brookes, Evidence of orbital reconstruction at interfaces in ultrathin $\text{La}_{0.67}\text{Sr}_{0.33}\text{MnO}_3$ films, *Phys. Rev. Lett.* **100**, 137401 (2008).
- [59] J. M. Pruneda, V. Ferrari, R. Rurli, P. B. Littlewood, N. A. Spaldin, and E. Artacho, Ferrodistortive instability at the (001) surface of half-metallic manganites, *Phys. Rev. Lett.* **99**, 226101 (2007).
- [60] F. Congiu, C. Sanna, L. Maritato, P. Orgiani, and A. Geddo Lehmann, Effect of natural homointerfaces on the magnetic properties of pseudomorphic $\text{La}_{0.7}\text{Sr}_{0.3}\text{MnO}_3$ thin film: Phase separation vs split domain structure, *J. Magn. Magn. Mater.* **420**, 88 (2016).
- [61] F. Cossu, U. Schwingenschlögl, G. Colizzi, A. Filippetti, and V. Fiorentini, Surface antiferromagnetism and incipient metal-insulator transition in strained manganite films, *Phys. Rev. B* **87**, 214420 (2013).
- [62] Notice that the ground state of the $n = 6$ case, corresponding to the $a^-a^-c^+$ tilting pattern, was neglected in our preliminary study of Ref. [56].
- [63] G. Kresse and J. Furthmüller, Efficient iterative schemes for ab initio total-energy calculations using a plane-wave basis set, *Phys. Rev. B* **54**, 11169 (1996).
- [64] G. Kresse and D. Joubert, From ultrasoft pseudopotentials to the projector augmented-wave method, *Phys. Rev. B* **59**, 1758 (1999).
- [65] J. P. Perdew, K. Burke, and M. Ernzerhof, Generalized gradient approximation made simple, *Phys. Rev. Lett.* **77**, 3865 (1996).
- [66] J. P. Perdew, K. Burke, and M. Ernzerhof, Generalized gradient approximation made simple [Phys. Rev. Lett. **77**, 3865 (1996)], *Phys. Rev. Lett.* **78**, 1396(E) (1997).
- [67] T. A. Mellan, F. Corà, R. Grau-Crespo, and S. Ismail-Beigi, Importance of anisotropic Coulomb interaction in LaMnO_3 , *Phys. Rev. B* **92**, 085151 (2015).
- [68] A. I. Liechtenstein, V. I. Anisimov, and J. Zaanen, Density-functional theory and strong interactions: Orbital ordering in Mott-Hubbard insulators, *Phys. Rev. B* **52**, R5467 (1995).
- [69] B. R. K. Nanda and S. Satpathy, Polar catastrophe, electron leakage, and magnetic ordering at the $\text{LaMnO}_3/\text{SrMnO}_3$ interface, *Phys. Rev. B* **81**, 224408 (2010).
- [70] B. R. K. Nanda and S. Satpathy, Spin-polarized two-dimensional electron gas at oxide interfaces, *Phys. Rev. Lett.* **101**, 127201 (2008).
- [71] J. Sun, A. Ruzsinszky, and J. P. Perdew, Strongly constrained and appropriately normed semilocal density functional, *Phys. Rev. Lett.* **115**, 036402 (2015).
- [72] The metaGGA SCAN functional was proven to be very successful in describing the physics of magnetic oxides [88].
- [73] J. H. Van Vleck, The Jahn-Teller effect and crystalline stark splitting for clusters of the form XY_6 , *J. Chem. Phys.* **7**, 72 (1939).
- [74] R. F. W. Bader, Atoms in molecules, *Acc. Chem. Res.* **18**, 9 (1985).
- [75] K. Momma and F. Izumi, VESTA3 for three-dimensional visualization of crystal, volumetric and morphology data, *J. Appl. Crystallogr.* **44**, 1272 (2011).
- [76] V. Wang, N. Xu, J.-C. Liu, G. Tang, and W.-T. Geng, VASPKIT: A user-friendly interface facilitating high-throughput computing and analysis using VASP code, *Comp. Phys. Commun.* **267**, 108033 (2021).
- [77] These sublattices reflect the different character of the magnetic coupling in the A-AFM ground state of bulk LaMnO_3 , since the interatomic exchange coupling is FM within each plane but AFM between planes.
- [78] J. Varignon, M. Bibes, and A. Zunger, Mott gapping in $3d\text{-ABO}_3$ perovskites without Mott-Hubbard interelectronic repulsion energy U , *Phys. Rev. B* **100**, 035119 (2019).
- [79] J. Varignon, M. Bibes, and A. Zunger, Origins versus fingerprints of the Jahn-Teller effect in d -electron ABX_3 perovskites, *Phys. Rev. Res.* **1**, 033131 (2019).
- [80] C. N. R. Rao, Charge, spin, and orbital ordering in the perovskite manganates, $\text{Ln}_{1-x}\text{A}_x\text{MnO}_3$ (Ln = rare earth, A = Ca or Sr), *J. Phys. Chem. B* **104**, 5877 (2000).
- [81] J. B. Goodenough, Theory of the role of covalence in the perovskite-type manganites $[\text{La}, \text{M(II)}]\text{MnO}_3$, *Phys. Rev.* **100**, 564 (1955).
- [82] J. Kanamori, Superexchange interaction and symmetry properties of electron orbitals, *J. Phys. Chem. Solids* **10**, 87 (1959).
- [83] J. B. Goodenough, *Magnetism and the Chemical Bond*, Interscience Monographs on Chemistry: Inorganic Chemistry Section (Interscience Publishers, New York, London, 1963).

- [84] R. Fetzter, B. Stadtmüller, Y. Ohdaira, H. Naganuma, M. Oogane, Y. Ando, T. Taira, T. Uemura, M. Yamamoto, M. Aeschlimann, and M. Cinchetti, Probing the electronic and spintronic properties of buried interfaces by extremely low energy photoemission spectroscopy, *Sci. Rep.* **5**, 8537 (2015).
- [85] I. Di Marco, A. Held, S. Keshavarz, Y. O. Kvashnin, and L. Chioncel, Half-metallicity and magnetism in the $\text{Co}_2\text{MnAl}/\text{CoMnVAl}$ heterostructure, *Phys. Rev. B* **97**, 035105 (2018).
- [86] O. I. Malyi and A. Zunger, False metals, real insulators, and degenerate gapped metals, *Appl. Phys. Rev.* **7**, 041310 (2020).
- [87] M. Baldini, T. Muramatsu, M. Sherafati, H. K. Mao, L. Malavasi, P. Postorino, S. Satpathy, and V. V. Struzhkin, Origin of colossal magnetoresistance in LaMnO_3 manganite, *Proc. Natl. Acad. Sci. USA* **112**, 10869 (2015).
- [88] J. Varignon, M. Bibes, and A. Zunger, Origin of band gaps in 3d perovskite oxides, *Nat. Commun.* **10**, 1658 (2019).
- [89] D. Li, K. Lee, B. Y. Wang, M. Osada, S. Crossley, H. Ryoung Lee, Y. Cui, Y. Hikita, and H. Y. Hwang, Superconductivity in an infinite-layer nickelate, *Nature (London)* **572**, 624 (2019).
- [90] J. Chang, J. Zhao, and Y. Ding, Hund-Heisenberg model in superconducting infinite-layer nickelates, *Eur. Phys. J. B* **93**, 220 (2020).
- [91] F. Lechermann, Multiorbital processes rule the $\text{Nd}_{1-x}\text{Sr}_x\text{NiO}_2$ normal state, *Phys. Rev. X* **10**, 041002 (2020).
- [92] Y. Wang, C.-J. Kang, H. Miao, and G. Kotliar, Hund's metal physics: From SrNiO_2 to LaNiO_2 , *Phys. Rev. B* **102**, 161118(R) (2020).
- [93] B. Kang, C. Melnick, P. Semon, S. Ryee, M. J. Han, G. Kotliar, and S. Choi, Infinite-layer nickelates as Ni-eg Hund's metals, *npj Quantum Mater.* **8**, 35 (2023).
- [94] A. Georges, L. de' Medici, and J. Mravlje, Strong correlations from Hund's coupling, *Annu. Rev. Condens. Matter Phys.* **4**, 137 (2013).
- [95] A. W. Tyler, A. P. Mackenzie, S. NishiZaki, and Y. Maeno, High-temperature resistivity of Sr_2RuO_4 : Bad metallic transport in a good metal, *Phys. Rev. B* **58**, R10107 (1998).
- [96] S.-C. Wang, H.-B. Yang, A. K. P. Sekharan, H. Ding, J. R. Engelbrecht, X. Dai, Z. Wang, A. Kaminski, T. Valla, T. Kidd, A. V. Fedorov, and P. D. Johnson, Quasiparticle line shape of Sr_2RuO_4 and its relation to anisotropic transport, *Phys. Rev. Lett.* **92**, 137002 (2004).